Insights into Machining of a β Titanium Biomedical Alloy from Chip Microstructures

Damon Kent[1,2,3,*], Rizwan Rahman Rashid[4,5], Michael Bermingham[2,3], Hooyar Attar[2], Shoujin Sun[4] and Matthew Dargusch[2,3]

[1] School of Science and Engineering, University of the Sunshine Coast, Maroochydore DC, QLD 4558, Australia; dkent@usc.edu.au

[2] Queensland Centre for Advanced Materials Processing and Manufacturing (AMPAM), The University of Queensland, St. Lucia, 4072, Australia; d.kent@uq.edu.au (D.K.); m.bermingham@uq.edu.au (M.B.); h.attar@uq.edu.au (H.A.); m.dargusch@uq.edu.au (M.B.)

[3] ARC Research Hub for Advanced Manufacturing of Medical Devices, St. Lucia, 4072, Australia

[4] School of Engineering, Faculty of Science, Engineering and Technology, Swinburne University of Technology, Victoria 3122, Australia; rrahmanrashid@swin.edu.au (R.R.); ssun@swin.edu.au (S.S.)

[5] Defence Materials Technology Centre, Victoria 3122, Australia

* Correspondence: dkent@usc.edu.au; Tel.: +61-5456-5267

Abstract: New metastable β titanium alloys are receiving increasing attention due to their excellent biomechanical properties and machinability is critical to their uptake. In this study machining chip microstructure have been investigated to gain an understanding of strain and temperature fields during cutting. For higher cutting speeds, ≥60 m/min, the chips have segmented morphologies characterised by a serrated appearance. High levels of strain in the primary shear zone promote formation of expanded shear band regions between segments which exhibit intensive refinement of the β phase down to grain sizes below 100 nm. The presence of both α and β phases across the expanded shear band suggests that temperatures during cutting are in the range of 400-600°C. For the secondary shear zone, very large strains at the cutting interface result in heavily refined and approximately equiaxed nanocrystalline β grains with sizes around 20-50 nm, while further from the interface the β grains become highly elongated in the shear direction. An absence of the α phase in the region immediately adjacent to the cutting interface indicates recrystallization during cutting and temperatures in excess of the 720°C β transus temperature.

Keywords: machining; titanium; temperature; strain; grain refinement; ultrafine; nanocrystalline

1. Introduction

β titanium alloys possess high strength to weight, excellent toughness, corrosion resistance and biocompatibility and so have excellent potential for a wide range of biomedical applications [1]. In the last decade, there has been significant focus on the development of a variety of new metastable β titanium alloys with lower Young's moduli approaching that of human bone. These alloys employ various combinations of elements to stabilise the body-centred cubic β titanium phase and can exhibit both shape memory and pseudoelastic behaviours [2,3]. A metastable Ti-Nb based β titanium alloy (Ti-25Nb-3Mo-3Zr-2Sn wt.%) with excellent mechanical and biological compatibility has recently been the subject of extensive research and development by the authors [4-6].

Biomedical components manufactured from titanium alloys typically require machining to achieve their required form, size and surface finish. However, machining can be problematic, particularly at high speeds, due to issues with build-up of heat at the cutting zone associated with titanium's relatively low thermal conductivity and high levels of chemical affinity which lead to

45 reaction with and 'sticking' to the cutting tool materials [7,8]. Typically, more than 70% of the heat
46 generated during machining is delivered to the cutting tool, intensifying the degree of chemical
47 interaction between the tool and workpiece [9,10]. For these reasons, most titanium alloys are
48 considered difficult to machine and much of the fabrication cost for geometrically complex
49 components may be due to machining. Hence, there is a strong incentive to better understand the
50 machining process to improve material removal for these alloys. A further driver to study these
51 processes comes from observations that the plastic deformation which takes place at the cutting
52 interface can also significantly influence cell viability and adhesion on metallic implant materials [11].
53   Previously, Rashid *et al.* studied the machinability of the Ti-25Nb-3Mo-3Zr-2Sn alloy including
54 cutting forces, temperatures and macroscopic chip characteristics [12,13]. For the solution treated and
55 aged Ti-25Nb-3Mo-3Zr-2Sn alloy, the main cutting force decreases from around 600 N at low cutting
56 speeds to around 430 N for speeds above 30 m/min, remaining constant at this level for speeds up to
57 almost 200 m/min. Measurements of the external chip surface temperatures in the cutting zone using
58 infrared thermography revealed that the temperatures are ≤300°C for low surface cutting speeds
59 (below 10 m/min), increasing markedly to more than 700°C for high surface cutting speeds
60 approaching 200 m/min [12]. The machining chips transition from a continuous form at low cutting
61 speeds to a segmented saw-tooth morphology for surface cutting speeds ≥60 m/min [13]. The
62 frequency of shear regions between individual sawtooth segments is associated with significant
63 fluctuations in component forces during machining which exacerbate tool wear.
64   The shear regions between the sawtooth segments are subject to localised, high strain rate, severe
65 plastic deformation at elevated temperatures. Due to the relatively small chip mass, the metal is
66 effectively quenched as it leaves the cutting zone preserving the as-machined microstructures. The
67 extreme deformation conditions may result in the formation of nano-crystalline and/or ultrafine-
68 grain microstructures of interest from the perspective of improving fundamental knowledge of
69 severe plastic deformation processes and their associated microstructures, as well as understanding
70 the cutting process. Schneider *et al.* used focussed ion beam (FIB) specimens from machining chips in
71 conjunction with transmission electron microscopy (TEM) to study the fine microstructural features
72 within the secondary deformation zone from cutting of the $\alpha+\beta$, Ti-6Al-4V (wt.%) alloy [14]. A
73 layered microstructure with fine grains near the cutting interface transitioning to coarse grains
74 toward the free surface was observed. A 10 nm thick recrystallised layer was present at the cutting
75 interface which adjoined a 20 nm thick amorphous layer. To the best of the author's knowledge,
76 similar high level characterisation of the fine scale deformation features formed during machining of
77 the increasingly important β titanium class of alloys has not yet been undertaken.
78   Recently, the deformation behaviours of the Ti-25Nb-3Mo-3Zr-2Sn (wt.%) alloy under high
79 strain rates (≈ 1000 s^{-1}), in the order of those encountered in machining, were studied using Split
80 Hopkinson Pressure Bar testing [15]. High strain rates alone did not significantly alter the
81 deformation mechanisms from those occurring under quasistatic strain conditions which involve
82 twinning ({332} <113> and {112} <111> twinning systems) as well as stress induced formation of the
83 α'' and ω phases. The strain hardening behaviour of the alloy was also strain rate insensitive under
84 these conditions due to limited adiabatic heating. However, at elevated deformation temperatures
85 ($\geq$300°C), the preferred deformation mechanism shifts to dislocation slip due to an increased relative
86 stability of the β phase promoting textural changes in the β grain orientation to those favouring slip,
87 i.e. the <001> and <111> fibre textures [16]. At elevated temperatures the yield stress also significantly
88 reduces due to the cessation of mechanical twinning in association with significant thermal softening.
89 These observations can inform the interpretation of the deformation processes taking place in the
90 chips during machining of the Ti-25Nb-3Mo-3Zr-2Sn alloy. Hence, the aim of this study is to
91 investigate deformation microstructures preserved in the machining chips and to relate these to the
92 strain and temperature fields present during machining. This will assist to better predict, model and
93 optimize machining operations involving β titanium biomedical alloys.
94

2. Materials and Methods

The investigated alloy has a nominal alloy composition of Ti-25Nb-3Mo-3Zr-2Sn (wt.%). A 25 kg ingot was produced by alloying commercially pure Ti sponge (99.5 wt.% purity), pure Zr bars (99.7 wt.%), pure Sn bars (99.9 wt.%), pure Mo powder (99.8 wt.%) and an intermediate Nb-47 wt.% Ti alloy. The alloy was melted twice by non-consumable arc melting to ensure chemical homogeneity and low levels of impurities. The ingots were forged and then hot rolled to produce cylindrical bars 33 mm in diameter. The bars were solution treated at 750 ˚C followed by air cooling and ageing at 450 ˚C for 2 h followed by air cooling.

The machining operation was performed on 3.5 hp Hafco Metal Master lathe, Model AL540. A carbide tool CNMX1204A2-SMH13A provided by Sandvik with +15° rake angle, – 6° inclination angle and entry angle of 45° was used to machine the Ti-25Nb-3Mo-3Zr-2Sn alloy under dry machining conditions. The machining operation under a constant feed rate of 0.19 mm/rev and constant depth of cut of 1 mm. Microstructural examination was performed on machining chips from cutting with surface cutting speeds around 90 m/min.

The machining chips were mounted and polished with the width direction of the chip perpendicular to the polished surface to reveal the serrated chip cross-section. The chips were etched with Kroll's reagent for observation with scanning electron microscopy (SEM) performed on a JEOL 6460 instrument equipped with backscatter detector. Hardness testing was conducted on polished specimens using a Struers Vickers microhardness tester. X-ray diffraction (XRD) was conducted using a D8 Advance X-Ray Diffractometer operated at 40KV and 30mA, equipped with a graphite monochromator, a Ni-filtered Cu Kα (λ=1.5406nm) source and a scintillation counter. Specimens for transmission electron microscopy (TEM) were prepared from transverse mounted sections of the machining chips by dual focused ion beam (FIB) milling using a Zeiss Auriga FIB-SEM. Sections approximately 100 nm in thickness were milled using a Ga+ beam with typical dimensions of 5 μm × 12 μm. The sections were attached to a C-section copper grid. The TEM was performed using a Philips Tecnai 20 FEG instrument.

3. Results

3.1. Workpiece Material

The solution treated and aged Ti-25Nb-3Mo-3Zr-2Sn alloy shown in Figure 1 (a) with XRD phase analysis in (b) consists of β grains with grain sizes in the order of 50 μm and lath shaped α precipitates (the dark phase in the SEM image) located primarily around the grain boundaries and protruding into the β grains. Some α laths are also present within the interior of the β grains. The solution treated and aged alloy has a hardness of 265 ∓ 5 HV, an ultimate tensile strength of approximately 800 MPa with typical tensile elongation of around 8% [12].
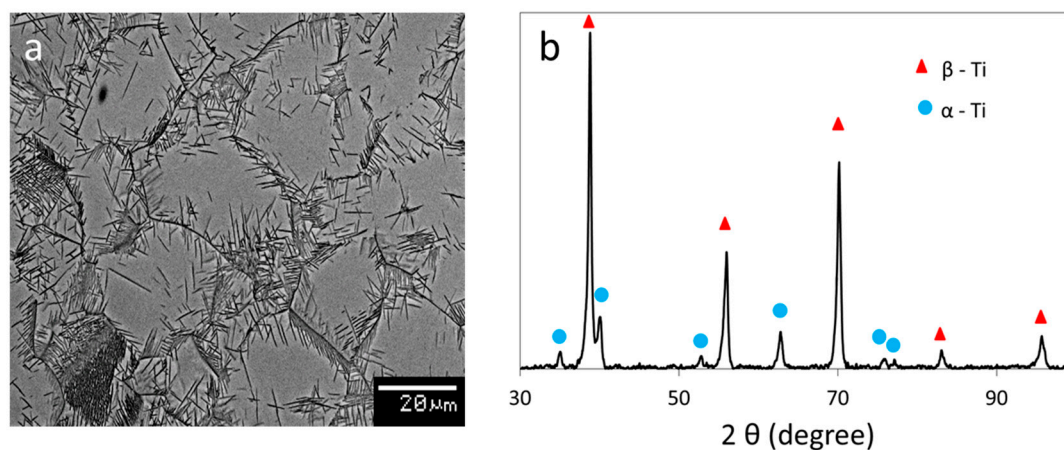
Figure 1. SEM image (a) and XRD spectrum (b) from the solution treated and aged workpiece material.

132　　*3.2. Machining Chip Characteristics*

133　　　　Cross-sections of Ti-25Nb-3Mo-3Zr-2Sn chips produced for cutting surface speeds of
134　　approximately 90 m/min are shown in Figure 2. Within this cutting regime the chips have segmented
135　　morphologies characterised by a serrated appearance with bands of severe plastic deformation,
136　　referred to herewith as expanded shear band regions, with more limited deformation in adjoining
137　　regions. According to previous research by the authors', at these cutting speeds the undeformed chip
138　　surface length, i.e. the distance between the regions of severe deformation measured from the top
139　　surface of the chip, are approximately 0.08 mm while the average chip thickness is approximately
140　　0.15 mm and the chip roughness ratio around 0.2 [12,13].

141　　　　The expanded shear band regions between the sawtooth chips feature extensive deformation as
142　　indicated in Figure 2(a), while the regions outside these bands are subject to more limited
143　　deformation and the original β grain structure of the workpiece material remains discernable,
144　　examples of which are indicated in Figure 2 (b). Typical microhardness values measured from within
145　　the expanded shear band regions were 398±15 HV, while adjoining regions with more limited
146　　deformation had hardness of around 292±8 HV which is still substantially harder than the initial
147　　starting material (265 ∓ 5 HV). As is also the case for formation of continuous chips, during formation
148　　of segmented chips deformation of the material occurs ahead of the tool in the region referred to as
149　　the primary shear zone. The transition from continuous to segmented chip morphologies, featuring
150　　thermoplastic instability-induced shear banding, emerges once the smooth chip flow becomes
151　　insufficient to dissipate the energy through homogeneous plastic flow [17]. The other significant area
152　　of deformation in the chip is the secondary shear zone shown in Figure 2 (c), which is the region
153　　adjoining the tool rake face during cutting. Hardness measurements from within the secondary shear
154　　zone were around 363±8 HV. However, it should be noted that the measurements were
155　　approximately 20μm from the outer edge of the chip which was as near to the cutting interface as
156　　could be reliably tested through microhardness measurements.

157　　　　To gain higher level understanding of the deformation microstructures formed during
158　　machining, TEM investigations were undertaken on samples from the expanded shear band regions
159　　formed in the primary deformation zone and from the secondary shear zone, shown in Figures 3 and
160　　4, respectively.
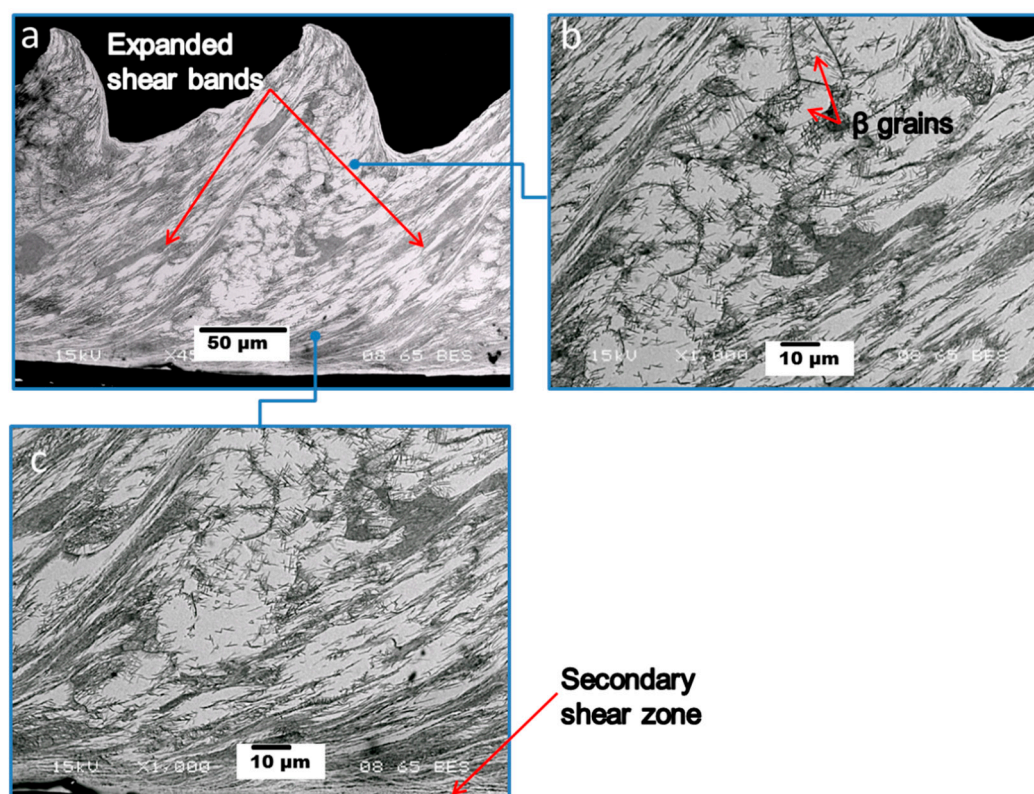
Figure 2. SEM of machining chip microstructure for surface cutting speed around 90 m/min: (a) Low magnification image of segmented chip morphology. (b) Undeformed chip region with original β grain structure of the workpiece material with in-tact β grains highlighted. (c) Higher magnification image of the secondary shear zone which adjoins the tool rake face during cutting.

3.3. TEM Analysis of Expanded Shear Band Region

A montage of bright field (BF) TEM images showing the typical microstructure within the expanded shear band region is presented in Figure 3 (a) and a selected area diffraction pattern (SADP) from this region is included inset. They reveal that the microstructure in the bands is highly refined, consisting of fine elongated β grains as the matrix phase interspersed with lath-like α precipitates (lighter contrast). The SAPD, indexed to the β and α phases, exhibits a continuous ring pattern characteristic of very fine and randomly oriented grains with large grain boundary misorientations. There is a gradient of deformation from the highly refined, smaller grains at the centre to more coarse grains at the left and right extremities. Some individual β grains can be identified (arrowed in Figure 3 (a)) due to dark strain contrast arising from high levels of dislocation activity. The arrowed β grains reveal the progression of refinement from the extremities to the interior. The β grains at the extremities have a diamond like shape with grain sizes in the order of 400-500 nm with α phase laths often sitting along their diagonal boundaries. Closer to the heavily refined central region, the β grains transition to an elongated form with grains around 20-50 nm in width and 300-400 nm in length, while the α laths with their long axis closely aligned to the length-wise axis of the β grains are 5-10 nm in width and 300-400 nm in length. In the most highly refined region, the β grain size is less than 100 nm.

Higher magnification BF and corresponding hollow cone dark field (HCDF) images from this highly refined region are presented in Figures 3 (b) and (c), respectively. They further reveal the fine β grains with considerable internal deformation structure as well as the lath-like α phase. A high magnification BF image showing the coarse diamond shaped β grains at the extremities of the deformation region is shown in Figure 3 (d).

188
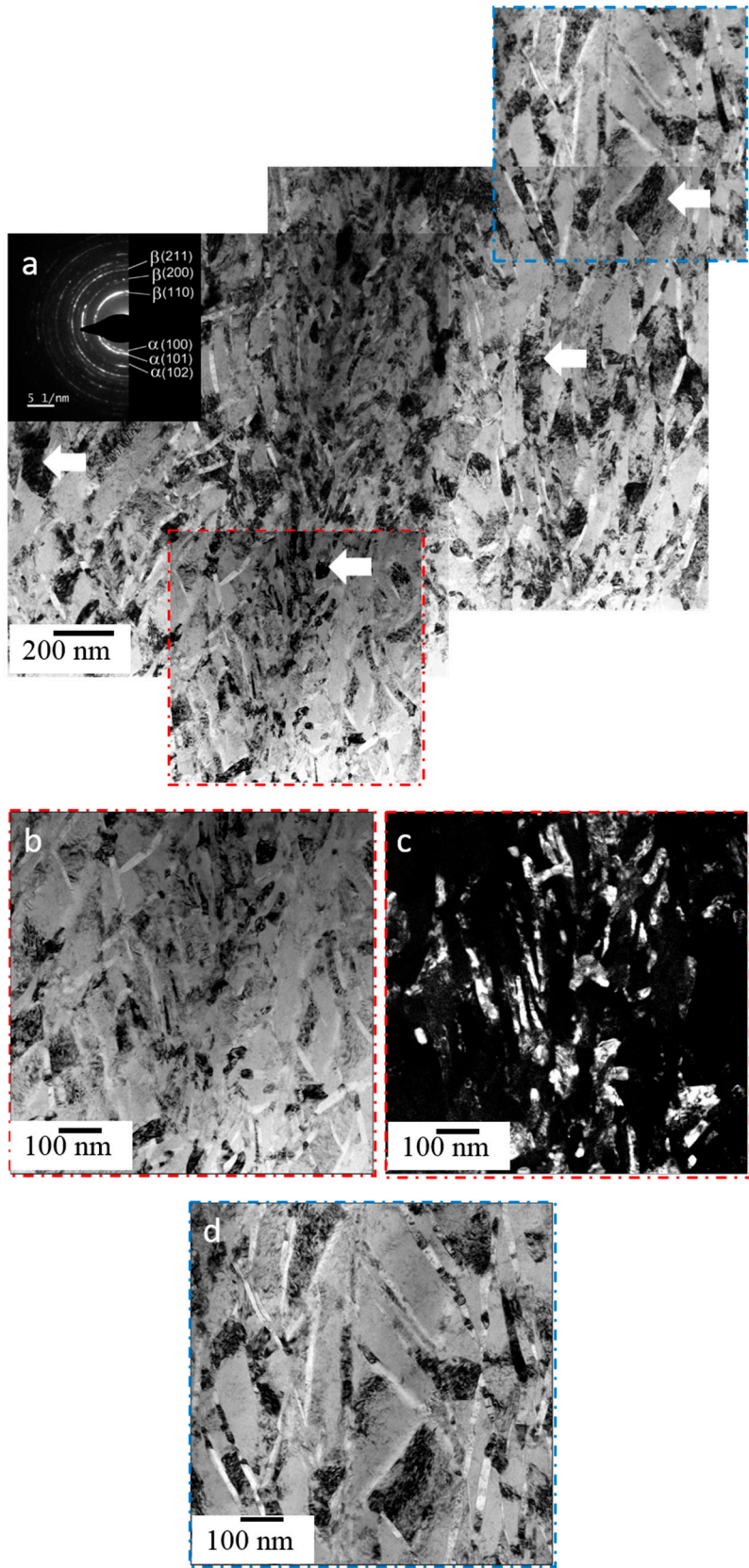
189 **Figure 3.** TEM from the expanded shear band region: (a) Montage of BF images with SADP inset
190 indexed to the β and α phases. (b) BF image and (c) corresponding HCDF image from the red dashed
191 region in (a) formed from β (110) and α (100), (002), (101) diffraction rings. (d) Higher magnification
192 BF image from the blue dashed region in (a).

193

194   *3.4. TEM Analysis of Secondary Shear Zone*

195   A series of TEM images from the secondary shear zone are presented in Figure 4. They reveal
196   the chip microstructure in the region immediately adjacent to the rake face (a), i.e. at the chip
197   extremity, and then moving incrementally into the chip interior, (b) and (c).

198   Figure 4 (a) shows a BF TEM image with SADP inset and corresponding HCDF image from the
199   region immediately adjacent to the rake face. The SADP exhibits a continuous ring pattern
200   characteristic of very fine and randomly oriented grains with reflections from the β phase only. The
201   BF image reveals a gradient of deformation from left to right from fine equiaxed grains immediately
202   adjacent to the cutting interface at the left with grain sizes around 30-50 nm to more elongated grains
203   50 to 100 nm in width and several hundreds of nm in length at the right further from the cutting
204   interface. A BF TEM image showing the significantly elongated β grains formed further from the
205   cutting interface (approximately 1-2 μm) and a corresponding HCDF formed from the β (110)
206   diffraction ring are shown in Figure 4 (b). Figure 4 (c) reveals the microstructure in the secondary
207   shear zone 5-10 μm from the cutting interface becomes less refined and consists of significantly larger,
208   elongated β grains with long lath-like α precipitates (lighter contrast). Again, some β grains exhibit
209   dark contrast arising from high levels of dislocation activity within their interiors. The SAPD from
210   this region exhibits a discontinuous ring pattern indicative of a less refined structure with reflections
211   from both the β and α phases.

212
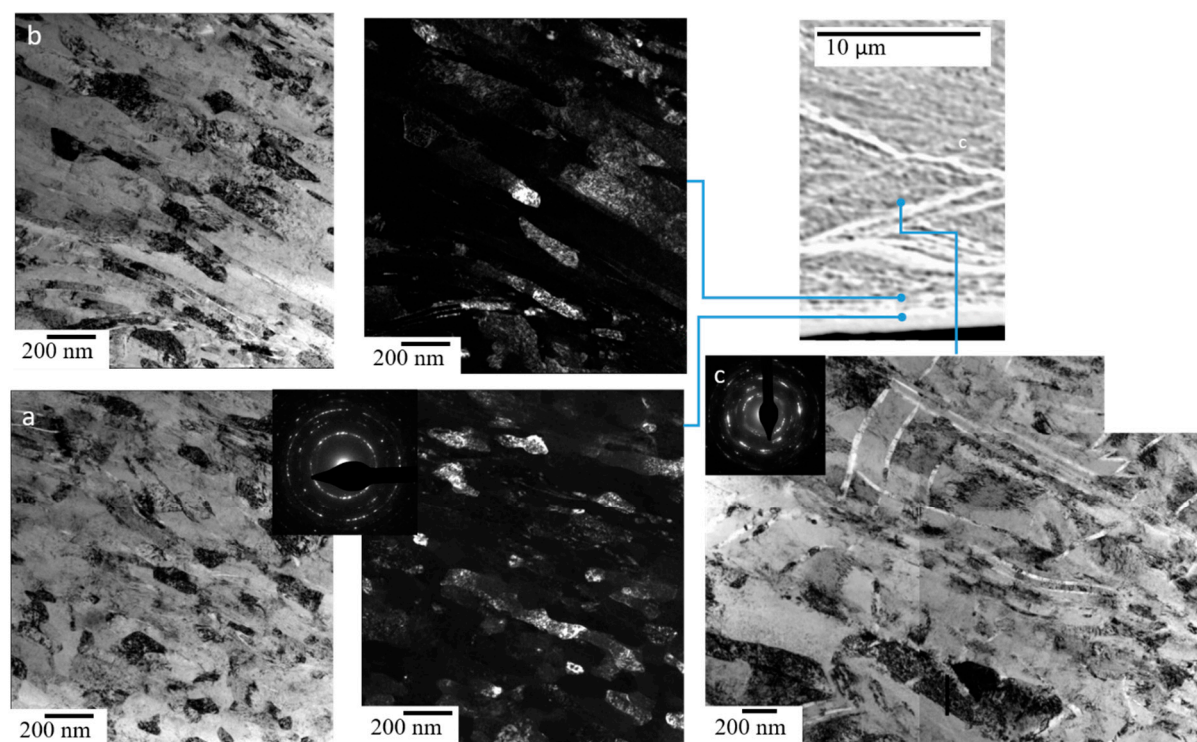
213   **Figure 4.** Series of TEM images from the secondary shear zone region immediately adjacent to the
214   rake face (a), i.e. the chip extremity, and incrementally further into the chip interior (b) and (c). (a) BF
215   image with SADP inset showing reflections almost entirely from the β phase and corresponding
216   HCDF image formed from the β (110) diffraction ring. (b) BF image and corresponding HCDF image
217   formed from β (110) diffraction ring. (c) Montage of BF images with SADP inset with reflections from
218   the β and α phases.

4. Discussion

220   The TEM characterisation revealed important details of the machining chip microstructures
221   which are linked to the deformation processes taking place in the chips during machining of the Ti-
222   25Nb-3Mo-3Zr-2Sn alloy. Significant differences were identified between the expanded shear bands

223   regions and the secondary shear zone which are discussed in respect to the influence of strain, heat
224   generation and temperatures encountered during cutting.
225   High levels of deformation in the expanded shear bands formed within the primary deformation
226   zone promote extensive localised refinement of the β phase to almost equiaxed grains with sizes
227   below 100 nm. Additionally, α phase laths frequently occupy the β grain boundaries, aligned to the
228   shear direction. This grain refinement consequently lead to an approximate 50% increase in hardness
229   from that of the starting material, primarily due to locally enhanced Hall-Petch strengthening [18]. In
230   regions adjacent to the fine equiaxed zone, there is a transition to firstly larger elongated β grains,
231   which according to the work of *Zhan et al.* [16] can be inferred to be the <001> and <111> fibre textures,
232   with α laths aligned to the shear direction, and then to larger diamond shaped β grains with α phase
233   often located on their diagonal axes. Across the entire width of the expanded shear band region this
234   variation in refinement suggests a cyclic process of formation such that the expanded shear band
235   consists of an accumulation of individual localised shear events. The presence of both β and α phases
236   across the entire expanded shear band region indicates that temperatures associated with adiabatic
237   heating during cutting do not exceed the β transus temperature of around 720°C for the Ti-25Nb-
238   3Mo-3Zr-2Sn alloy [19]. The high density of α phase laths in this region suggest that dynamic
239   precipitation may also take place in conjunction with the deformation. This suggests that
240   temperatures during cutting are likely in the range of 400-600°C [20].
241   Shear localisations are often observed in titanium alloys subject to dynamic loading associated
242   with their low heat conductivity and high adiabatic shearing sensitivity [21]. Chip formation occurs
243   by concentrated shear within the deformation band and the microstructural refinement is attributed
244   to the large shear strains imposed. The formation of the shear regions is linked to substantial
245   reductions in the yield stress which occur during cutting due to substantial thermal softening of the
246   Ti-25Nb-3Mo-3Zr-2Sn alloy at elevated temperatures [16]. Under the momentum diffusion-based
247   shear band evolution model, a highly localised primary shear band forms at the centre of the primary
248   deformation zone and large deformation occurs inside the shear band as the localised shear
249   deformation proceeds [22]. Subsequent thermal softening enables relaxation of the stress within the
250   shear band and the stress relaxation further propagates into the surrounding undisturbed material
251   giving rise to momentum diffusion and broadening of the deformation region as the expanded shear
252   band regions evolve.
253   In comparison to the highly localised shear bands observed in cutting of other titanium alloys
254   [23-26], the expanded shear band regions observed for the Ti-25Nb-3Mo-3Zr-2Sn alloy are relatively
255   diffuse. Under the current cutting conditions, for the Ti-25Nb-3Mo-3Zr-2Sn alloy these zones are
256   around 100 μm in width and of a similar magnitude to that of the regions with more limited
257   deformation. An increase in hardness of around 10% from the starting material in regions between
258   the expanded shear bands indicates that deformation in the primary shear zone is not entirely
259   confined to the expanded shear band regions. Additionally, increased temperatures during cutting
260   may also promote further α phase precipitation in these regions of more limited deformation which
261   would also increase hardness.
262   For the secondary shear zone, strains at the cutting interface can be very large (>5) [27] typically
263   leading to formation of ultrafine and/or nanocrystalline grain structures. The level of strain and hence
264   refinement decays with increasing distance from the cutting interface across the secondary shear
265   zone, which is in the order of 15-20 μm in width for the Ti-25Nb-3Mo-3Zr-2Sn alloy. At the cutting
266   interface the β grains are heavily refined and approximately equiaxed with very fine nanocrystalline
267   grain sizes around 20-50 nm while further from the interface, approximately 1-2 μm, the β grains
268   become highly elongated in the shear direction with grains in the order of 100 nm in width and 0.5
269   to 1 μm in length. Again it can be inferred that the elongated grains are aligned to the <001> and <111>
270   fibre textures [16]. An absence of the α phase in the equiaxed and elongated β grain regions of the
271   secondary shear zone indicates that recrystallization takes place during cutting and temperatures are
272   in excess of the alloy's 720°C β transus temperature while subsequent rates of cooling are sufficiently
273   high to preserve the single phase β microstructure. At 5-10 μm from the cutting interface a mixture
274   of larger elongated β grains and long α laths are observed and the hardness is enhanced by more

275   than 30% over that of the starting material. This can be attributed to the effects of significant β phase
276   refinement resulting from deformation during cutting which enhances Hall-Petch strengthening as
277   well as dynamic precipitation taking place due to the elevated temperatures during cutting. The α
278   laths tend to have thinner, longer morphologies than those observed within the expanded shear band
279   region which is potentially due to the influence of comparatively higher temperatures and strains in
280   this region, which favour growth of precipitates over nucleation through dynamic precipitation
281   effects.
282   As the temperature and intensity of strain decrease across the secondary shear zone as a function
283   of the distance from the cutting interface, the microstructures observed reflect their differing
284   thermomechanical histories. The variations observed in the microstructure across the secondary
285   deformation zone for the Ti-25Nb-3Mo-3Zr-2Sn alloy are largely consistent with those reported for
286   adiabatic shear bands formed in titanium alloys [21,28,29] involving a progression to finer, more
287   equiaxed grains in the region of most intense deformation, in this case at the cutting interface [14].
288   Previously, Rashid *et al.* [12] used infrared thermography to measure the maximum
289   temperatures at the back surface of the chips in the cutting region during machining of the Ti-25Nb-
290   3Mo-3Zr-2Sn alloy. They reported the average temperatures to be 540-600°C for surface cutting
291   speeds of 80-100 m/min for the solution treated and aged alloy. However, as the cutting edge was
292   covered by the chip, the temperatures reported were those from the cutting zone at the external
293   surface of the chip, i.e. on the opposite side to the cutting interface. Therefore, the actual temperature
294   at the interface between the cutting face of the tool and the chip may be substantially higher than
295   those reported. Additionally, infrared thermography temperature measurements are acknowledged
296   to be subject to substantial error [30,31] and temperatures in the cutting zone are far from uniform,
297   being typically characterised by regions of high temperature gradient [32,33]. The microstructural
298   characterisation of the chips gives some insight into the degree of these temperature gradients for
299   machining of the solution treated and aged Ti-25Nb-3Mo-3Zr-2Sn alloy. For the chip, the significant
300   sources of heat are; in the primary deformation zone due to plastic work associated with shear and
301   in the secondary deformation zone due to work done in deformation of the chip and in association
302   with sliding friction at the tool-chip interface.
303   Based on the assumption that all mechanical work is converted to heat, the cutting forces can be
304   applied to estimate heat generation during cutting. In this case, the heat generated in the primary
305   deformation zone, Q_s, can be calculated from [32]:

$$Q_s = W_c = F_V \cdot V \qquad (1)$$

306   where F_V is the tangential cutting force and V is the cutting velocity.
307   The amount of heat generated due to work done in the secondary deformation zone along the
308   tool rake face is calculated from the frictional energy given by:

$$Q_r = \frac{F_{fr} \cdot V}{\lambda} \qquad (2)$$

309   where F_{fr} is the total shear force acting on the rake face and λ is the chip thickness ratio. The
310   shear force can be calculated from:

$$F_{fr} = F_V \sin(\alpha) + F_S \cos(\alpha) \qquad (3)$$

311   where F_S is the feed force and α is the rake angle. An estimate of the heat generated in the primary
312   and secondary deformation zone made from the above equations using the cutting forces reported
313   by Rashid *et.al.* [12] with a tangential cutting force, $F_V = 450\ N$, a feed force, $F_S = 240\ N$, a cutting
314   velocity, $V = 90\ m/min$, a chip thickness ratio, $\lambda = \frac{0.19\ mm}{0.15\ mm}$ and a rake angle $\alpha = 9°$ yields heat
315   generation of approximately 40 kW in the primary deformation zone and 22 kW in the secondary
316   shear zone. From this analysis, the heat generated in the secondary shear zone for cutting of the Ti-
317   25Nb-3Mo-3Zr-2Sn alloy is proportionately quite high at around 55% of that in the primary
318   deformation zone. For context, Tay *et al.* observe that typically the total heat generation due to plastic

319   deformation and frictional sliding in the secondary deformation zone for continuous chips from a
320   non-abrasive material at medium cutting speeds is around 20 to 30 % of the heat generated in the
321   primary cutting zone [34].
322   During cutting heat is removed by the chip, the tool and the workpiece and some of the heat
323   generated at the shear plane (primary shear zone) is transferred to the tool-chip interface. Hence, the
324   temperature in the chip in the region adjacent to the tool rake face rises due to the combination of
325   heat from the primary and secondary shear zones. Predictions of the temperature fields in the chip
326   on the basis of heat generation are complex and have been the subject of various analytical and
327   numerical investigations involving modelling of heat conduction, kinematics, geometries and energy
328   aspects of the machining process. Others have attempted to measure temperature both at the cutting
329   interface zone and across the chip, tool and workpiece through the methods including embedded
330   thermocouples, radiation pyrometers and metallographic techniques [34,35]. In general, the highest
331   temperatures are reportedly near the tool-chip interface in the secondary deformation zone. This is
332   consistent with the microstructural analysis of the Ti-25Nb-3Mo-3Zr-2Sn alloy chips which indicated
333   that temperatures in this region were in excess of 720°C during cutting.

5. Conclusions

335   Ultrafine grain microstructures formed by severe plastic deformation during machining of the
336   solution treated and aged Ti-25Nb-3Mo-3Zr-2Sn biomedical β titanium alloy have been investigated
337   by TEM analyses of specimens obtained by FIB from transverse section of chips. The investigations
338   have revealed that:
339   1. High levels of deformation in the primary shear zone promote extensive refinement of the β
340   phase within expanded shear band regions approximately 100μm in width to almost equiaxed grains
341   with sizes below 100 nm in regions of intense deformation, while α phase laths frequently occupy the
342   grain boundaries aligned to the shear direction. There is a transition to firstly elongated β grains and
343   then to larger diamond shaped β grains in adjoining regions of less intense deformation. The presence
344   of a high density of α phase laths across the entire expanded shear band region suggests that
345   temperatures in this region are likely in the range of 400-600°C during cutting.
346   2. For the secondary shear zone, large strains at the cutting interface result in recrystallised,
347   approximately equiaxed grains with nanocrystalline grain sizes around 20-50 nm, while further (1-2
348   μm) from the interface the β grains become highly elongated in the shear direction with grains in the
349   order of 100 nm in width and 0.5 to 1 μm in length. At the cutting interface, an absence of the α phase
350   indicates that the temperatures exceed the alloy's 720°C β transus temperature. At 5-10 μm, from the
351   cutting interface a mixture of large elongated β grains and long α phase laths are observed. The
352   microstructural variation across the secondary shear zone reflects the decay of strain and temperature
353   away from the cutting interface.
354   3. The microstructural characterisation of the chips infers information on the temperature fields
355   present across the chips during cutting. The highest cutting temperatures occur within the secondary
356   shear zone at the cutting interface, associated with proportionately high levels of heat generation due
357   to deformation and friction.

Author Contributions: Conceptualization, D.K., M.D., S.S. and M.B.; Methodology, D.K.; Investigation, D.K., R.R. and H.A.; Writing-Original Draft Preparation, D.K.; Writing-Review & Editing, R.R., M.B. and S.S.; Project Administration, M.D.; Funding Acquisition, D.K. M.B. and M.D.

Funding: This research was funded by the Australian Research Council (ARC) Research Hub for Advanced Manufacturing of Medical Devices (IH150100024).

Acknowledgments: The authors acknowledge the facilities, and the scientific and technical assistance, of the Australian Microscopy & Microanalysis Research Facility at the Centre for Microscopy and Microanalysis, The University of Queensland and at the Australian Centre for Microscopy & Microanalysis at the University of Sydney.

Conflicts of Interest: The authors declare no conflict of interest.

References

1. Long, M.; Rack, H.J. Titanium alloys in total joint replacement - a materials science perspective. Biomaterials 1998, 19, 1621-1639.
2. Niinomi, M. Mechanical biocompatabilities of titanium alloys for biomedical applications. J. Mech. Behav. Biomed. Mater. 2008, 1, 30-42.
3. Ping, D.H.; Mitarai, Y.; Yin, F.X. Microstructure and shape memory behavior of a Ti-30Nb-3Pd alloy. Scr. Mater. 2005, 52, 1287-1291.
4. Yu, Z.; Wang, G.; Ma, X.Q.; Dargusch, M.S.; Han, J.Y.; Yu, S. Development of biomedical near beta titanium alloys. Mater. Sci. Forum: 4th International Light Metals Technology Conference 2009, 618-619.
5. Kent, D.; Wang, G.; Yu, Z.; Dargusch, M.S. Pseudoelastic behaviour of a β Ti-25Nb-3Zr-3Mo-2Sn alloy. Mater. Sci. Eng. A 2010, 527, 2246-2252.
6. Kent, D.; Wang, G.; Yu, Z.; Ma, X.; Dargusch, M.S. Strength enhancement of a biomedical titanium alloy through a modified accumulative roll bonding technique. J. Mech. Behav. Biomed. Mater. 2011, 4, 405-416.
7. Rahman, M.; Wong, Y.S.; Zareena, A.R. Machinability of titanium alloys. JSME Int. J., Ser. C 2003, 46, 107-115.
8. Yang, X.; Liu, C.R. Machining titanium and its alloys. Mach. Sci. Technol. 1999, 3, 107-139.
9. Ezugwu, E.O.; Wang, Z.M. Titanium alloys and their machinability - a review. J. Mater. Process. Technol. 1997, 68, 262-274.
10. Machado, A.R.; Wallbank, J. Machining of titanium and its alloys. A review. Proc. Inst. Mech. Eng., Part B 1990, 204, 53-60.
11. Uzer, B.; Toker, S.M.; Cingoz, A.; Bagci-Onder, T.; Gerstein, G.; Maier, H.J.; Canadinc, D. An exploration of plastic deformation dependence of cell viability and adhesion in metallic implant materials. J. Mech. Behav. Biomed. Mater. 2016, 60, 177-186.
12. Rahman Rashid, R.A.; Sun, S.; Wang, G.; Dargusch, M.S. Machinability of a near beta titanium alloy. Proc. Inst. Mech. Eng., Part B 2011, 225, 2151-2162.
13. Rashid, R.A.R.; Sun, S.; Wang, G.; Dargusch, M.S. Experimental investigation of various chip parameters during machining of the Ti25Nb3Mo3Zr2Sn beta titanium alloy. Adv. Mat. Res., 2013; Vol. 622, pp 366-369.
14. Schneider, J.; Dong, L.; Howe, J.Y.; Meyer Iii, H.M. Microstructural characterization of Ti-6Al-4V metal chips by focused ion beam and transmission electron microscopy. Metall. Mater. Trans. A 2011, 42, 3527-3533.
15. Zhan, H.; Zeng, W.; Wang, G.; Kent, D.; Dargusch, M. On the deformation mechanisms and strain rate sensitivity of a metastable β Ti-Nb alloy. Scr. Mater. 2015, 107, 34-37.
16. Zhan, H.; Wang, G.; Kent, D.; Dargusch, M. The dynamic response of a metastable β Ti-Nb alloy to high strain rates at room and elevated temperatures. Acta Mater. 2016, 105, 104-113.
17. Ye, G.G.; Xue, S.F.; Ma, W.; Dai, L.H. Onset and evolution of discontinuously segmented chip flow in ultra-high-speed cutting Ti-6Al-4V. Int. J. Adv. Manuf. Tech. 2017, 88, 1161-1174.
18. Hughes, G.D.; Smith, S.D.; Pande, C.S.; Johnson, H.R.; Armstrong, R.W. Hall-petch strengthening for the microhardness of twelve nanometer grain diameter electrodeposited nickel. Scr. Metall. 1986, 20, 93-97.
19. Zhentao, Y.; Lian, Z. Influence of martensitic transformation on mechanical compatibility of biomedical β type titanium alloy tlm. Mater. Sci. Eng. A 2006, 438–440, 391-394.
20. Kent, D.; Pas, S.; Zhu, S.; Wang, G.; Dargusch, M.S. Thermal analysis of precipitation reactions in a ti–25nb–3mo–3zr–2sn alloy. Appl. Phys. A: Mater. Sci. Process. 2012, 107, 835-841.
21. Wang, B.; Wang, X.; Li, Z.; Ma, R.; Zhao, S.; Xie, F.; Zhang, X. Shear localization and microstructure in coarse grained beta titanium alloy. Mater. Sci. Eng. A 2016, 652, 287-295.
22. Ye, G.G.; Xue, S.F.; Jiang, M.Q.; Tong, X.H.; Dai, L.H. Modeling periodic adiabatic shear band evolution during high speed machining Ti-6Al-4V alloy. Int. J. Plast. 2013, 40, 39-55.
23. Arrazola, P.J.; Garay, A.; Iriarte, L.M.; Armendia, M.; Marya, S.; Le Maître, F. Machinability of titanium alloys (Ti6Al4V and Ti555.3). J. Mater. Process. Technol. 2009, 209, 2223-2230.
24. Joshi, S.; Pawar, P.; Tewari, A.; Joshi, S.S. Effect of β phase fraction in titanium alloys on chip segmentation in their orthogonal machining. CIRP-JMST 2014, 7, 191-201.
25. Sun, S.; Brandt, M.; Dargusch, M.S. Characteristics of cutting forces and chip formation in machining of titanium alloys. Int. J. Mach. Tool. Manu. 2009, 49, 561-568.
26. Dargusch, M.S.; Sun, S.; Kim, J.W.; Li, T.; Trimby, P.; Cairney, J. Effect of tool wear evolution on chip formation during dry machining of ti-6al-4v alloy. Int. J. Adv. Manuf. Tech. 2018, 126, 13-17.

422   27.   Oxley, P.L.B. Mechanics of machining. Ellis Horwood: New York, 1989.
423   28.   Zhan, H.; Zeng, W.; Wang, G.; Kent, D.; Dargusch, M. Microstructural characteristics of adiabatic shear
424   localization in a metastable beta titanium alloy deformed at high strain rate and elevated temperatures.
425   Mater. Charact. 2015, 102, 103-113.
426   29.   Yang, Y.; Jiang, F.; Zhou, B.M.; Li, X.M.; Zheng, H.G.; Zhang, Q.M. Microstructural characterization and
427   evolution mechanism of adiabatic shear band in a near beta-ti alloy. Mater. Sci. Eng. A 2011, 528, 2787-2794.
428   30.   Davies, M.A.; Ueda, T.; M Saoubi, R.; Mullany, B.; Cooke, A.L. On the measurement of temperature in
429   material removal processes. CIRP Ann. Manuf. Technol. 2007, 56, 581-604.
430   31.   Lane, B.; Whitenton, E.; Madhavan, V.; Donmez, A. Uncertainty of temperature measurements by infrared
431   thermography for metal cutting applications. Metrologia 2013, 50, 637-653.
432   32.   Abukhshim, N.A.; Mativenga, P.T.; Sheikh, M.A. Heat generation and temperature prediction in metal
433   cutting: A review and implications for high speed machining. Int. J. Mach. Tool. Manu. 2006, 46, 782-800.
434   33.   Sutter, G.; Ranc, N. Temperature fields in a chip during high-speed orthogonal cutting—an experimental
435   investigation. Int. J. Mach. Tool. Manu. 2007, 47, 1507-1517.
436   34.   Tay, A.O.; Stevenson, M.G.; de Vahl Davis, G. Using the finite element method to determine temperature
437   distributions in orthogonal machining. I Inst. Mech. Eng. (Lond) Proc.1974, 188, 627-638.